Journal of Natural Gas Science and Engineering 33 (2016) 885–897

Contents lists available at ScienceDirect

Journal of Natural Gas Science and Engineering

journal homepage: www.elsevier.com/locate/jngse

A coupled extended finite element approach for modeling hydraulic fracturing in consideration of proppant

Fang Shi [a], XiaoLong Wang [a], Chuang Liu [a], He Liu [b], HengAn Wu [a, *]

[a] CAS Key Laboratory of Mechanical Behavior and Design of Materials, Department of Modern Mechanics, University of Science and Technology of China, Hefei, Anhui, 230027, China

[b] PetroChina Research Institute of Petroleum Exploration & Development, 20 Xueyuan Road, Haidian District, Beijing, 100083, China

ARTICLE INFO

Article history:
Received 28 January 2016
Received in revised form
26 April 2016
Accepted 13 June 2016
Available online 16 June 2016

Keywords:
Hydraulic fractures
Fluid-solid coupling
XFEM
Proppant transport
Proppant packing

ABSTRACT

Due to its influence on the stress field around the propped fractures in horizontal well and the final conductivity of the created fracture network, the transport and packing of proppant plays a significant role in hydraulic fracturing. Therefore, it is important to describe the distribution of proppant in fractures and to accurately model the propped fractures. To this aim, a two-dimensional fully coupled model based on the extended finite element method (XFEM) is established, which takes into account some crucial physical processes, including rock deformation, fracturing fluid flow, fracturing fluid leak-off, propagation of fractures, proppant transport and proppant packing. The fluid-solid coupling equations are solved by the Newton-Raphson method and the proppant transport is evaluated by the upwind scheme. The hexagonal close packing of proppant is used to calculate the width of propped fracture. By taking advantage of the characteristic features of XFEM, an efficient strategy to model the propped fracture is proposed by directly enforcing the displacement boundary conditions on relevant enriched degrees of freedom without adding additional elements. The proposed coupled approach is validated by comparison with existing literature. The results of the sequential fracturing show that the propagation path of the subsequently created fracture is strongly affected by the boundary conditions (i.e., sliding contact, filled with constant pressure fluid, or propped open by proppant) imposed on the previously propped fracture, and the proposed XFEM-based strategy to model the propped fracture is an accurate and efficient alternative. Further sensitivity analysis reveals that the fracture spacing and the proppant concentration of the injected slurry also have significant influence on propagation path of the subsequently created fracture. The advantages of XFEM make the proposed coupled approach an attractive tool for the design of hydraulic fracturing.

1. Introduction

Hydraulic fracturing is a widely applied technology for enhancing production of conventional and unconventional oil and gas reservoirs. It usually involves using a high-pressure fluid to pressurize the wellbore until fractures emerge, which is followed by continuous injection of thousands gallons of fluid into emerged fractures to drive them to extend farther into the formation. During the injection process, proppant is added to the fracturing fluid at the right time to prevent fracture surfaces from fully closing when the fluid pressure drops (Britt, 2012). For a better understanding of hydraulic fracturing, many researchers have devoted their efforts to numerical simulation studies of this problem.

Many numerical methods have been adopted for the simulation of hydraulic fracturing, among which the most widely used are the displacement discontinuity method (DDM) (Kresse et al., 2013; McClure and Horne, 2013; Sesetty and Ghassemi, 2015; Weng et al., 2014; Zhang and Jeffrey, 2006), the finite element method (FEM) (Carrier and Granet, 2012; Chen, 2012; Guo et al., 2015a, 2015b; Papanastasiou, 1999; Wangen, 2011), and the recently developed extended finite element method (XFEM) (Dahi-Taleghani and Olson, 2011; Gordeliy and Peirce, 2013; Lecampion, 2009; Mohammadnejad and Khoei, 2013). The DDM is developed on the basis of linear elastic fracture mechanics as well as a variant of the conventional boundary element method (Wrobel and Aliabadi, 2002), and is suitable to model fracture. The finite

* Corresponding author.
E-mail address: wuha@ustc.edu.cn (H. Wu).

http://dx.doi.org/10.1016/j.jngse.2016.06.031
1875-5100/

element method is a flexible, effective and widely used numerical method. However, numerical simulation of large number of fractures in unconventional reservoirs using FEM is time consuming due to the remeshing process as fractures propagate. Some improvement strategies have been proposed to solve the shortcomings of FEM, among which the most effective one is the extended finite element method.

The XFEM (Daux et al., 2000; Moës et al., 1999; Stolarska et al., 2001; Sukumar and Prevost, 2003) allows fractures to propagate along arbitrary paths without explicit remeshing, thus the computational cost can be dramatically reduced in comparison to the conventional finite element method. The XFEM has not been applied to model hydraulic fracturing until recently. The XFEM was adopted to investigate the solution of hydraulic fracturing problem considering pressure inside the fracture and special tip enrichment functions (Lecampion, 2009). Then, the XFEM was used to model hydraulic fracture propagation accounting for the effect of the natural fracture (Dahi-Taleghani and Olson, 2011). Afterwards, a fully coupled XFEM model was established to describe the hydraulically driven fracture growth in porous formation (Mohammadnejad and Khoei, 2013). Recently, Gordeliy and Peirce (2013) developed two different schemes for fracture with fluid lag and fracture with singular tip pressure. Overall, in view of the flexibility of XFEM, many researchers are focusing on the development of XFEM-based hydraulic fracturing simulators.

Proppant transport plays an important role in hydraulic fracturing, especially for sequential fracturing where previously created fractures are propped by the injected proppant. This is because the opening of the propped fracture in a horizontal well will cause the stress reorientation in its adjacent region, which will influence the propagation paths of subsequent fractures. On the other hand, the final conductivity of the created fracture network is also related to the distribution of proppant. Over the years, some studies have been done for the modeling of proppant transport in a single planar fracture. A numerical model together with an adaptive finite element procedure was developed to simulate the proppant distribution in an expanding hydraulic fracture by Ouyang et al. (1997). A model based on finite difference method and finite volume method was developed to simulate fracture propagation, closure, contact and proppant transport by Zhou et al. (2014). Recently, a model capable of capturing both gravitational settling and tip screen-out effects was developed by Dontsov and Peirce (2015). In these studies, their research efforts are mainly focused on proppant transport in a single fracture, but not on the stress interference induced by the propped fractures for multistage fracturing. In practice, during the process of sequential fracturing, the subsequently created fractures will deviate from the desired propagation paths and turn to non-planar fractures due to the stress field induced by the propped fractures. The DDM-based unconventional fracture model (UFM) (Kresse et al., 2013; Weng et al., 2014) is able to model the creation of complex fracture network considering the proppant transport, but the width of fracture is calculated from the analytical solution. Recently, Sesetty and Ghassemi (2015) studied the effect of stress interference in the horizontal well based on DDM, but the proppant transport and the width of the propped fracture had not been considered in their model. In fact, the width of the propped fracture is directly related to the distribution of proppant (Bose et al., 2015). On the other hand, when dealing with hydraulic fracturing problems, the XFEM is a promising choice because fractures are completely independent of the mesh topology in XFEM and remeshing can be avoided. Therefore, it would be very useful and necessary to develop an XFEM-based model for hydraulic fracturing in consideration of proppant.

In this paper, we propose a two-dimensional fully coupled model which is able to consider a variety of physical processes, including fluid flow in fractures, fluid leak-off into surrounding rock formation, mechanical deformation of fracture walls induced by fluid pressure, propagation of fractures, proppant transport in fractures and proppant packing. This paper is focused on the proppant, so some other important topics such as the impact of in-situ natural fractures (Dahi-Taleghani and Olson, 2011; Guo et al., 2015a; Kresse et al., 2013; Weng et al., 2014) and the production performance (Sun and Schechter, 2015) are not discussed in the present study. In this paper, the proposed model is first validated by comparison with existing literature. Then, the simulation of sequential fracturing in a horizontal well is carried out to investigate the influence of proppant on stress distribution and propagation path of fracture. Further, sensitivity analysis is performed to investigate the effect of fracture spacing and proppant concentration of the injected slurry for sequential fracturing.

2. Problem formulation and numerical modeling method

Consider a fracture Γ_{frac} filled with high-pressure incompressible fluid in a domain Ω, as illustrated in Fig. 1. The boundary of the domain is Γ and the outwards unit normal vector of Γ is represented by $\boldsymbol{n}_{\Gamma}$. The prescribed tractions $\boldsymbol{t}$ and the displacements $\overline{\boldsymbol{u}}$ are imposed on the boundary Γ_t and Γ_u, respectively. The two surfaces of the fracture are expressed by the positive "+" and the negative "−" signs, and the outwards unit normal vectors of the positive and negative faces are donated by $-\boldsymbol{n}_{\Gamma_{frac}}$ and $\boldsymbol{n}_{\Gamma_{frac}}$, respectively. Slurry (for convenience, fluids with and without proppant are both named as slurry in this paper) are injected at the rate of $Q(t)$ at different time instants t. We define a one-dimensional curvilinear coordinate system (donated by s) along the fracture, and the coordinate origin is placed at the injection point.

Some assumptions are made for simplicity. In general, the slurry is not a Newtonian fluid. However, in terms of computer simulation, slurry can be treated as Newtonian fluid for simplicity (Adachi et al., 2007; Hammond, 1995; Tomac and Gutierrez, 2013). Besides, we assume that the propagation of the fracture is a quasi-static process, and there is no fluid lag between the fracture tip and the fluid front. The gravitational settling of proppant, which might not be particularly significant for the relatively lightweight proppant or the relatively high viscosity slurry (Mansoor, 2015), is not taken into account. In addition, the proppant flow back after the injection is finished is also not taken into consideration in this paper.

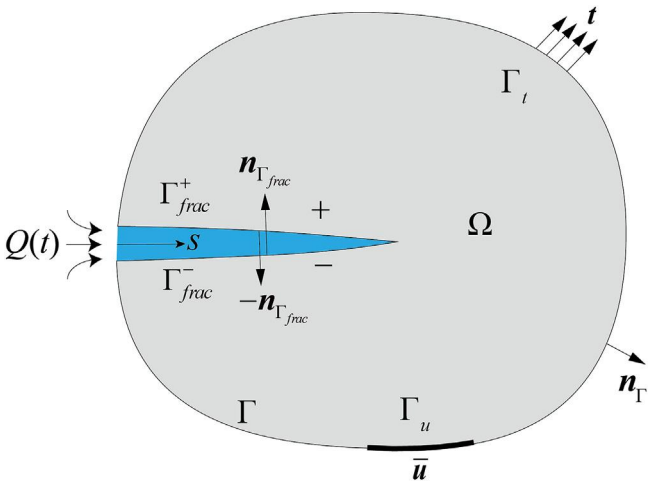

Fig. 1. Illustration of a domain containing a fracture filled with high-pressure fluid.

2.1. Rock deformation and fracture propagation criterion

The equilibrium equation of the domain can be expressed as

$$\nabla\cdot\boldsymbol{\sigma}=\mathbf{0} \tag{1}$$

where $\boldsymbol{\sigma}$ is the stress tensor, and $(\nabla\cdot)$ is the divergence operator. The boundary conditions can be expressed as

$$\begin{cases} \boldsymbol{u}=\overline{\boldsymbol{u}} & \text{on} \quad \Gamma_u \\ \boldsymbol{\sigma}\cdot\boldsymbol{n}_\Gamma=\boldsymbol{t} & \text{on} \quad \Gamma_t \\ \boldsymbol{\sigma}\cdot\boldsymbol{n}_{\Gamma_{frac}}=p\boldsymbol{n}_{\Gamma_{frac}} & \text{on} \quad \Gamma_{frac} \end{cases} \tag{2}$$

where p is the fluid pressure. The elastic constitutive law is adopted to characterize the material property of rock formation, that is

$$\boldsymbol{\sigma}=\boldsymbol{D}:\boldsymbol{\varepsilon} \tag{3}$$

where $\boldsymbol{D}$ is the elasticity tensor, and $\boldsymbol{\varepsilon}$ represents the strain tensor.

The maximum hoop tensile stress criterion (Erdogan and Sih, 1963) is used to determine when and how the fracture propagates. This criterion assumes that the propagation direction is along a direction normal to the maximum hoop tensile stress, and when the equivalent stress intensity factor K_e is greater than or equal to the fracture toughness of the rock formation, K_{IC}, the fracture will propagate. In this paper, the domain forms of the interaction integral method (Moran and Shih, 1987) are employed to determine the stress intensity factors K_I and K_{II}. The equivalent stress intensity factor K_e can be written as

$$K_e=\cos\frac{\theta}{2}\left(K_I\cos^2\frac{\theta}{2}-\frac{3K_{II}}{2}\sin\theta\right) \tag{4}$$

where θ is the fracture propagation angle in the local fracture tip coordinate system and can be determined by

$$\theta=2\arctan\left(\frac{-2K_{II}/K_I}{1+\sqrt{1+8(K_{II}/K_I)^2}}\right) \tag{5}$$

2.2. Slurry flow and proppant transport

The one-dimensional flow of slurry and proppant in the fracture must satisfy the mass conservation equations. For any point s in the fracture, these equations can be expressed as

$$\frac{\partial w}{\partial t}+\frac{\partial q_s}{\partial s}+g_L(s,t)-Q(t)\delta(s)=0 \tag{6}$$

$$\frac{\partial wc}{\partial t}+\frac{\partial q_p}{\partial s}-c_{inj}(t)Q(t)\delta(s)=0 \tag{7}$$

where w donates the width of the fracture; c is the proppant volumetric concentration, which is defined as the fraction of the volume occupied by the proppant; q_s and q_p are the slurry and proppant fluxes, respectively; $Q(t)$ and $c_{inj}(t)$ are the injection rate of slurry and the proppant volumetric concentration at the injection point, respectively; $g_L(s,t)$ donates the fluid leak-off into the surrounding rock formation. Note that c in Eq. (7) is a normalized concentration averaged over the fracture width.

Carter's model (Carter, 1957) is adopted to simulate the leak-off process of fluid, that is

$$g_L(s,t)=\frac{2C_L}{\sqrt{t-t_0(s)}} \tag{8}$$

where C_L is the Carter's leak-off coefficient, and $t_0(s)$ is the time when the leak-off process starts for point s.

Under the lubrication theory, slurry and proppant fluxes within the fracture can be given according to Poiseuille's law (Batchelor, 1967) along with Hammond's work (1995):

$$q_s=-\frac{w^3}{12\mu(0)}f_s\frac{\partial p}{\partial s} \tag{9}$$

$$q_p=-\frac{w^3}{12\mu(0)}f_p\frac{\partial p}{\partial s} \tag{10}$$

where $\mu(0)$ is the viscosity of the slurry without proppant, f_s and f_p are non-dimensional functions defined as

$$f_s=\frac{2\mu(0)}{3\mu(c)} \tag{11}$$

$$f_p=\frac{2\mu(0)}{3\mu(c)}c \tag{12}$$

where $\mu(c)$ is the effective viscosity of the slurry, which is given as

$$\mu(c)=\mu(0)\left(1-\frac{c}{\widehat{c}}\right)^{-m} \tag{13}$$

In Eq. (13), the exponent m and the saturation concentration $\widehat{c}$ are set as 2 and 0.6, respectively, in this paper.

Substituting Eq. (9) into Eq. (6) leads to the Reynolds equation

$$\frac{\partial w}{\partial t}-\frac{\partial}{\partial s}\left(k\frac{\partial p}{\partial s}\right)+g_L(s,t)-Q(t)\delta(s)=0 \tag{14}$$

where k is the permeability of the fracture, and

$$k=\frac{w^3}{12\mu(0)}f_s \tag{15}$$

For a hydraulic fracture, Eq. (14) can be solved with the following initial and boundary conditions

$$\begin{cases} w(s,0)=0 \\ w(s_{tip},t)=0 \\ q_s(0,t)=Q(t) \\ q_s(s_{tip},t)=0 \end{cases} \tag{16}$$

and the global mass conservation equation

$$\int_0^{s_{tip}} w\mathrm{d}s=\int_0^t Q(t)\mathrm{d}t-\int_0^{s_{tip}}\int_0^t g_L(s,t)\mathrm{d}s\mathrm{d}t \tag{17}$$

In the above equations, s_{tip} represents the location of the fracture tip.

2.3. The extended finite element method and discretization

To discrete the equilibrium equation, the extended finite element method is employed to approximate the displacement field $\boldsymbol{u}$. In XFEM, to consider the displacement jump across fracture surfaces and the singular displacement field around the fracture tip,

the displacement $\boldsymbol{u}$ for any point $\boldsymbol{x}$ can be approximated by

$$\boldsymbol{u}(\boldsymbol{x}) = \sum_{i\in S_{all}} N_i^u(\boldsymbol{x})\boldsymbol{u}_i + \sum_{j\in S_{frac}} N_j^u(\boldsymbol{x})H(\boldsymbol{x})\boldsymbol{a}_j + \sum_{k\in S_{tip}} N_k^u(\boldsymbol{x})\sum_{l=1}^{4} F_l(\boldsymbol{x})\boldsymbol{b}_k^l \tag{18}$$

where S_{all} is the set of all nodes, S_{frac} is the nodes set whose support domains are divided into two parts by the fracture, S_{tip} is the nodes set whose support domains are partially cut by the fracture. $N_i^u(\boldsymbol{x})$, $N_j^u(\boldsymbol{x})$ and $N_k^u(\boldsymbol{x})$ are the standard finite element shape functions. $\boldsymbol{u}_i$ is the conventional nodal displacement vector. $\boldsymbol{a}_j$ and $\boldsymbol{b}_k^l$ ($l = 1,4$) are the nodal enriched degree of freedom (DOF) vectors. $H(\boldsymbol{x})$ and $F_l(\boldsymbol{x})$ are enrichment functions of the discontinuous displacement field across the fracture surfaces and the singular displacement field around the fracture tip, respectively. $H(\boldsymbol{x})$ is usually taken as the signed Heaviside function (Sukumar and Prevost, 2003), and $F_l(\boldsymbol{x})$ takes the general form

$$\{F_l(r,\theta)\}_{l=1}^4 = \left\{\sqrt{r}\sin\frac{\theta}{2}, \sqrt{r}\cos\frac{\theta}{2}, \sqrt{r}\sin\theta\sin\frac{\theta}{2}, \sqrt{r}\sin\theta\cos\frac{\theta}{2}\right\} \tag{19}$$

where (r, θ) defines the polar coordinate system with the origin at the fracture tip. The enriched nodes for a typical hydraulic fracture are illustrated in Fig. 2. By substituting the approximation equation (Eq. (18)) into the weak form of the equilibrium equation, we can obtain the discretized form of the equilibrium equation (more details can be seen in Appendix A).

$$\boldsymbol{KU} - \boldsymbol{QP} - \boldsymbol{F} = \boldsymbol{0} \tag{20}$$

In order to approximate the one-dimensional pressure field $p(s,t)$ inside a hydraulic fracture, the hydraulic fracture interface Γ_{frac} is discretized into fluid elements using linear shape functions. The nodes of the fluid elements are arranged at the intersection points of hydraulic fractures and edges of solid elements, as shown in Fig. 2. The approximation of fluid pressure field can be written as

$$p(s) = \sum_{i\in S_{hf}} N_i^p(s)p_i \tag{21}$$

where $N_i^p(s)$ represents the shape function of pressurep_i for node i.

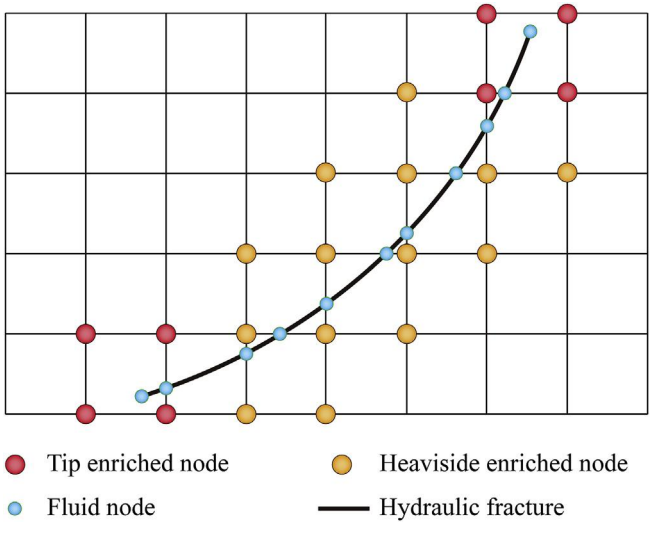

Fig. 2. Schematic of fluid nodes and enriched nodes for a hydraulic fracture.

By substituting Eq. (21) into the weak form of the Reynolds equation, we can obtain the discretized flow equation (details can be seen in Appendix A), that is

$$\boldsymbol{Q}^T\Delta\boldsymbol{U} + \Delta t\boldsymbol{HP} + \Delta t\boldsymbol{S} - \Delta t\boldsymbol{G} = \boldsymbol{0} \tag{22}$$

2.4. Widths of propped fracture

Fig. 3 show the statuses of proppant inside a fracture at different phases of fracturing. We idealistically assume that the proppant has the same diameter and is in close contact with each other after the hydraulic pressure is released (Fig. 3(b)). Moreover, the embedment of proppant into fracture faces is ignored. We suppose that the proppant is placed in a multilayer pattern and in the idealized hexagonal close packing (HCP) form (Rivers et al., 2012; Steinhaus, 1999) in three-dimensional space. Thus, for any point s inside a propped fracture, the propped width $w_p(s)$ can be determined by

$$w_p(s) = \frac{w_o(s)c(s)}{\eta} \tag{23}$$

where $w_o(s)$ is the width of point s before the fracture starts to close, and η represents the so-called packing density and equals $\pi/3\sqrt{2}$ (about 0.74) for the hexagonal close packing form (Steinhaus, 1999).

After the fracture is propped, the normal distance between two fracture surfaces is restricted to $w_p(s)$. Meanwhile, the relative movement between the two surfaces in the tangential direction is still free. Therefore, for an enriched node, whose degrees of freedom in x and y directions are donated by a_x and a_y, respectively, the multipoint constraint condition (Chandrupatla et al., 2012) of a_x and a_y can be obtained according to a simple geometric relation, namely

$$\beta_1 a_x + \beta_2 a_y = \beta_0 \tag{24}$$

where $\beta_1 = -\sin\gamma$, $\beta_2 = \cos\gamma$, β_0 approximately equals $w_o(s)/2$ when a relatively fine mesh is used, and γ is the inclination of the propped fracture. The above constraint condition can be simply imposed on the system equations by employing the penalty function method (Chandrupatla et al., 2012).

2.5. Coupling approach

In order to precisely simulate hydraulic fracturing, many physical processes such as fluid flow inside fractures, fluid leak-off into surrounding rock formation, mechanical deformation of fracture surfaces, growth of fractures, proppant transport and proppant packing are taken into account in the proposed model.

As discussed above, the discretized coupled equilibrium equation and flow equation can be written as

$$\begin{cases} \boldsymbol{KU} - \boldsymbol{QP} - \boldsymbol{F} = \boldsymbol{0} \\ \boldsymbol{Q}^T\Delta\boldsymbol{U} + \Delta t\boldsymbol{HP} + \Delta t\boldsymbol{S} - \Delta t\boldsymbol{G} = \boldsymbol{0} \end{cases} \tag{25}$$

The above coupled equations can be solved by the Newton-Raphson method (details can be found in Appendix B). The proppant transport equation (Eq. (7)) can be coupled at the end of each time step as follows. Firstly, the proppant concentration of the last time step (donated by c_{last}) is used to calculate the effective viscosity $\mu(c_{last})$ according to Eq. (13). Then, after some manipulations, Eq. (7) can be rewritten as

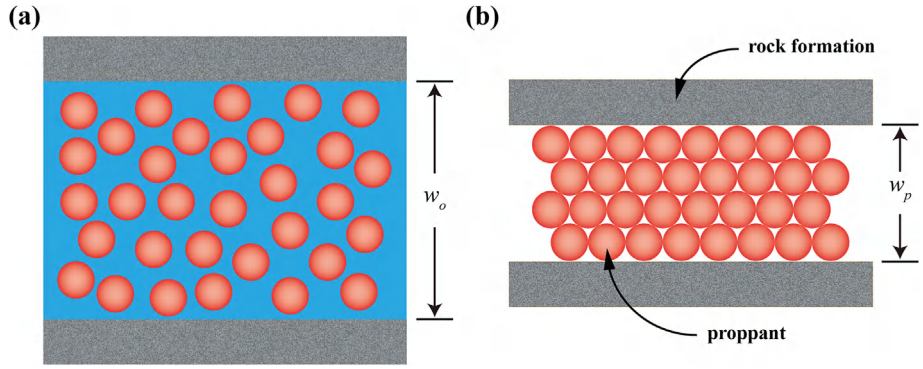

Fig. 3. (a) Illustration of proppant inside a fracture before the fracture is propped. (b) Illustration of multilayer-packed proppant after the fracture is propped.

$$\frac{\partial c}{\partial t} + \chi \frac{\partial c}{\partial s} = 0 \tag{26}$$

where χ equals $-\frac{w^2}{24\mu(C_{gst})}\frac{\partial p}{\partial s}$. The above linear convection equation can be solved typically by the upwind scheme (Hirsch, 1990), namely

$$c_i^{\tilde{n}+1} = c_i^{\tilde{n}} - \Delta\tilde{t}\left(\chi^+ c_s^- + \chi^- c_s^+\right) \tag{27}$$

where $\tilde{n}$ and $\Delta\tilde{t}$ represent the step number and the step size of the upwind scheme, respectively, and $\chi^+ = \max(\chi, 0)$, $\chi^- = \min(\chi, 0)$, $c_s^+ = (c_{i+1}^n - c_i^n)/\Delta s$, $c_s^- = (c_i^n - c_{i-1}^n)/\Delta s$. The above scheme is stable if the following condition is satisfied (Hirsch, 1990)

$$\left|\chi \frac{\Delta\tilde{t}}{\Delta s}\right| \le 1 \tag{28}$$

Eventually, the coupled problem under consideration can be solved by three main steps during each time step. Step (i): determine the state of each fracture, that is, whether it is driven by fluid, propped by proppant or a proppant-free fracture. Step (ii): iteratively solve the coupling equations between propagation of fractures and fluid flow using the Newton-Raphson method. Step (iii): solve the proppant transport using the upwind scheme, and then update the locations of the fracture tips according to the maximum hoop tensile stress criterion. The flow chart of the coupled approach is shown in Fig. 4.

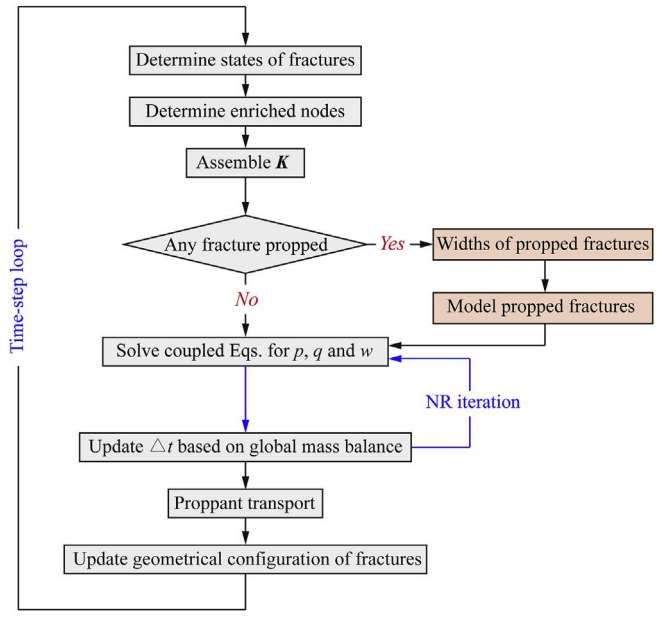

Fig. 4. Flow chart of the coupled approach.

3. Results and discussions

In this section, we will first verify the proposed model and then simulate sequential fracturing problems in a horizontal well. The in-house program used in this paper is written in Fortran 90. A direct solver known as LAPACK (Chen et al., 2003) is utilized to solve the linear system of the coupled equations.

3.1. Verification

3.1.1. Verification of the fluid-solid coupling model against analytical solutions

In this section, we consider the case of no proppant and no leak-off, then the coupled equations (Eq. (25)) can be verified by comparison with analytical solutions which depend on the dimensionless fracture toughness K_m of the KGD model (Hu and Garagash, 2010). K_m can be written as

$$K_m = 4\left(\frac{2}{\pi}\right)^{1/2}\frac{K_{IC}(1-\nu^2)}{E}\left[\frac{E}{12\mu Q(1-\nu^2)}\right]^{1/4} \tag{29}$$

where E is the elastic modulus and ν is the Poisson's ratio of the rock formation. The fracture propagation regime is viscosity-dominated when $K_m < 1$ and is toughness-dominated if $K_m > 4$. The analytical solutions of viscosity-dominated case and toughness-dominated case are given in detail by Detournay (2004), and they are both used to verify the proposed scheme through an example with different parameters listed in Table 1. For the large viscosity case K_m equals 0.0176 and for the large toughness case K_m equals 4.9443, as given in Table 1. The fracture is positioned at the center of the

Table 1
Material properties and fracturing parameters.

Parameter	Units	Value	
		Large viscosity	Large toughness
Elastic modulus E	GPa	20	20
Poisson's ratio ν	–	0.2	0.2
Fracture toughness K_{IC}	MPa $m^{1/2}$	0.1	5.0
Injection rate Q	m^2/s	0.001	0.001
Viscosity μ	Pa s	1.0	0.001
Dimensionless toughness K_m	–	0.0176	4.9443

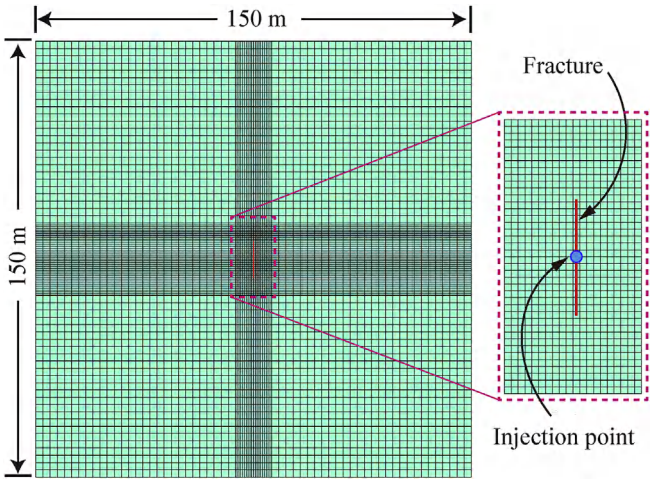

Fig. 5. Finite element mesh of the model.

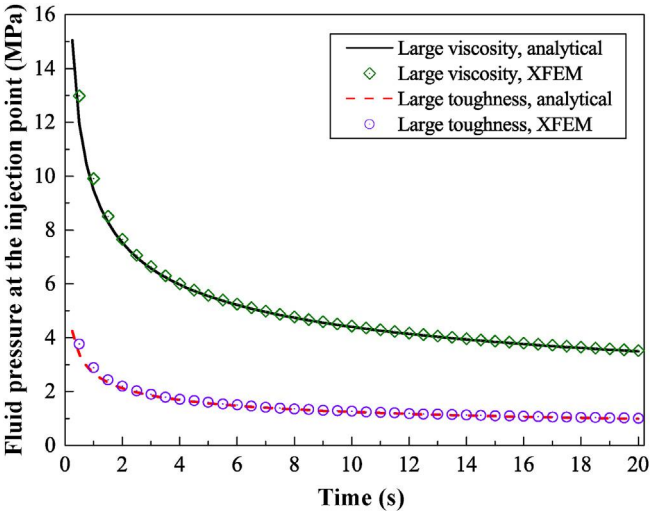

Fig. 6. Comparison of fluid pressures at the injection point from XFEM and analytical solution at various instants.

model which has dimensions of 150 × 150 m. The finite element mesh of the model which contains 6840 elements is shown in Fig. 5. The size of elements around the fracture is 0.5 × 0.5 m.

The variations of fluid pressure at the injection point are shown in Fig. 6. Fracture width profiles at different moments are shown in Fig. 7. The corresponding results of the analytical model are also shown for comparison in Figs. 6 and 7. It can be seen that the proposed approach is able to predict satisfactory results.

3.1.2. *Verification of proppant transport in a single fracture against existing literature*

In the previous section, we have verified that the proposed method can correctly deal with the coupling between fluid flow and solid deformation without considering proppant. However, despite some assumptions have been made, there is no available analytical solution when the proppant transport is considered. In this section, we will calculate the proppant distribution in a single fracture. We will analyze the effects of the maximum proppant concentration (c_{max}) and the leak-off coefficient C_L on the simulation results, and then compare the results with existing literature. The properties used in this section are the same as the large viscosity case in Table 1, except a smaller and dynamic slurry viscosity

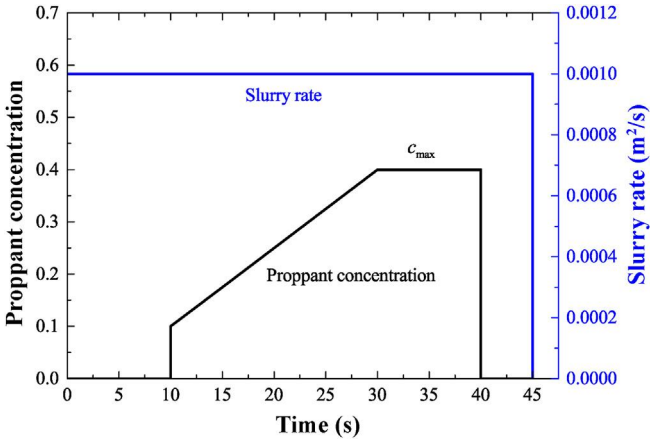

Fig. 8. Time-dependent slurry rate and proppant concentration at the injection point.

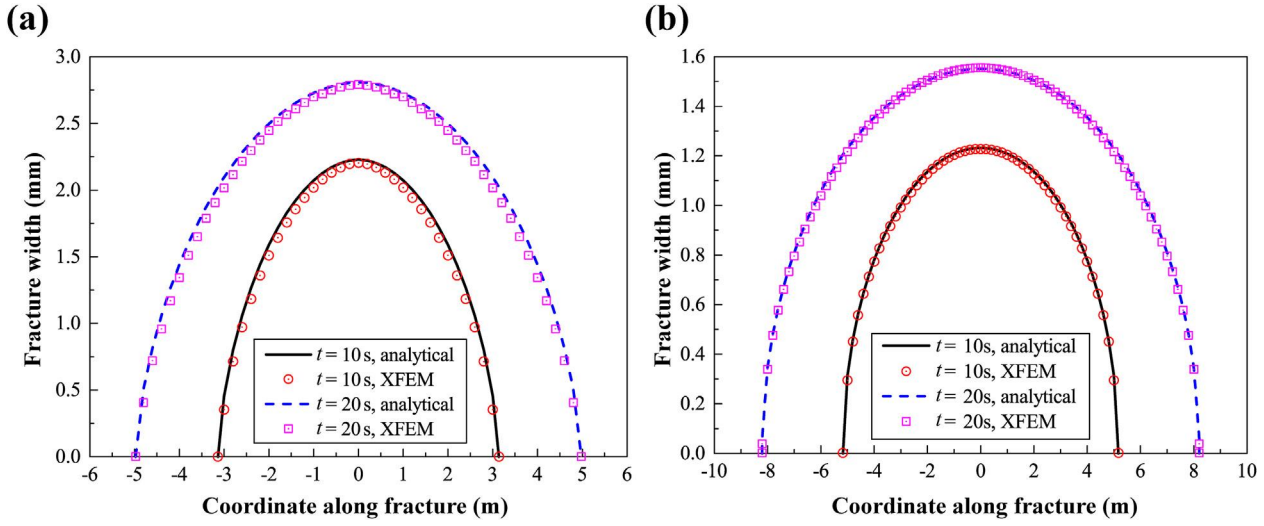

Fig. 7. Comparison of fracture widths from XFEM and analytical solution at different moments (t = 10 s and t = 20 s) for the large viscosity case (a) and the large toughness case (b).

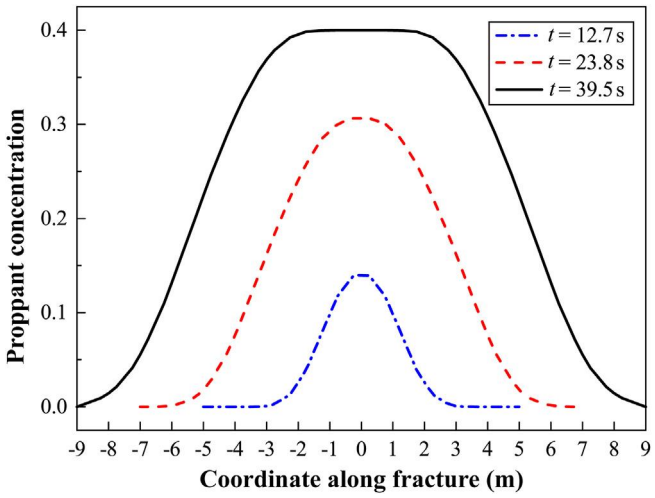

Fig. 9. Proppant concentration distributions at different time instants, $t = 12.7$ s, 23.8 s and 39.5 s.

the pore space of the surrounding formation. This conclusion is supported by other studies (Daneshy, 1978; Queipo et al., 2002), as they both provide evidence for the increase in proppant concentration caused by leak-off.

3.2. Simulation of sequential fracturing in a horizontal well with different boundary conditions on previously created fracture

This section is devoted to investigate the stress perturbation created by the propped fracture for the sequential fracturing in a transverse horizontal well, and to compare the effects of boundary conditions imposed on the previously created fracture. As shown in Fig. 11, the previous two stages (i.e., Stage-1 and Stage-2) of a sequential fracturing are simulated. The spacing between Stage-1 and Stage-2 fractures is 10 m. To make a comparison, three different boundary conditions (BCs) for Stage-1 fracture are considered after the injection of the Stage-2 fracture is started, as schematically shown in Fig. 11. BC (1) is the sliding contact boundary condition, which means that there is no proppant inside the fracture and no fluid pressure remains. BC (2): the fracture

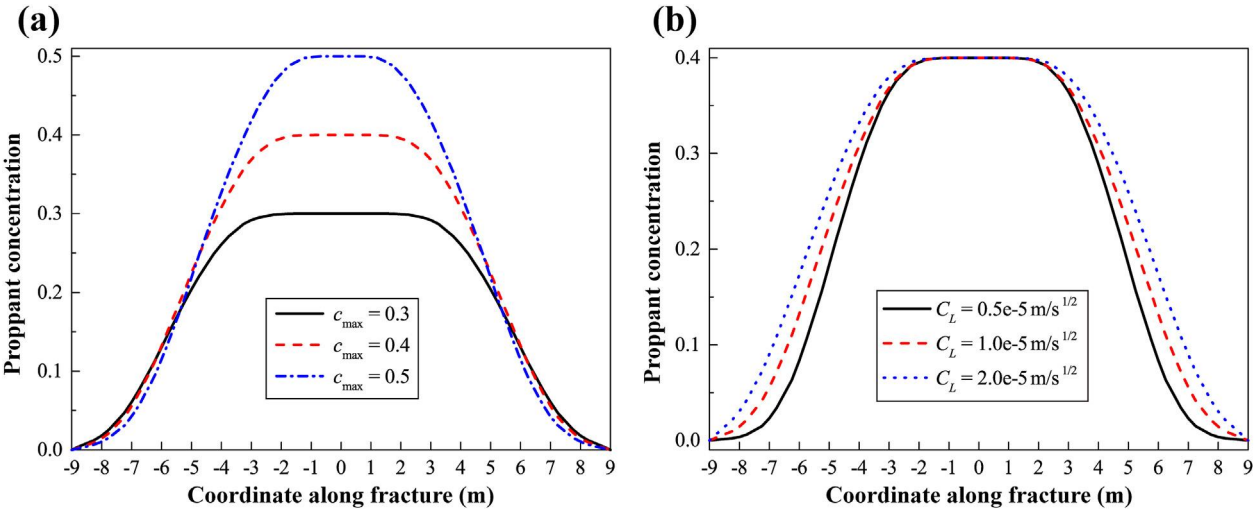

Fig. 10. (a) Proppant concentration distributions for different c_{max}. C_L equals 1×10^{-5} m/s$^{1/2}$. (b) Proppant concentration distributions along the fracture for different leak-off coefficients C_L. c_{max} equals 0.4.

($\mu(0)$ equals 0.1 Pa s). Moreover, the time-dependent slurry rate and proppant concentration at the injection point are graphically shown in Fig. 8, in which the maximum concentration (c_{max}) is 0.4. The model size and the mesh are the same as those in Section 3.1.1. The leak-off of fracturing fluid is considered and the leak-off coefficient C_L is taken as 1×10^{-5} m/s$^{1/2}$.

Fig. 9 shows the proppant distributions at different time instants ($t = 12.7$ s, 23.8 s and 39.5 s) when the fracture reaches to a length of 10 m, 14 m and 18 m, respectively. It is apparent that as the injection of proppant, the proppant concentration in the fracture increases continuously. The concentration of proppant around the injection point is larger than that near the fracture tips. A sensitivity analysis has been conducted by changing c_{max} and C_L separately. As can be seen from Fig. 10(a) in which the length of the fracture is 18 m, the proppant concentration increases with the maximum proppant concentration c_{max}, which is physically reasonable. Fig. 10(b) shows the effect of the leak-off coefficients C_L on proppant distribution when the fracture propagates to a length of 18 m. It is clearly seen that the proppant concentration increases with C_L, because more fluid of the slurry leaks through fracture surfaces into surfaces are subjected to a constant fluid pressure (Liu et al., 2015). BC (3): the fracture is propped open by proppant at different concentrations. For BC (2), we assume that the fluid pressure redistributes uniformly along the fracture after the injection is completed. The value of the redistributed constant pressure can be simply calculated according to the conservation of mass law. BC (3) can be realized by the method described in Section 2.4.

The material properties and fracturing parameters for each fracturing stage, including the slurry rate and the proppant concentration for BC (3), are kept the same as in the previous section where c_{max} and leak-off coefficient are taken as 0.4 and 1×10^{-5} m/s$^{1/2}$, respectively. The in-situ stresses in x and y directions (i.e., σ_{min} and σ_{max}, respectively, as shown in Fig. 11) are 3 and 5 MPa, respectively. The model has the same dimensions as depicted in the previous sections. The target length of these two fractures is 20 m. The size of elements around the fractures is 0.5×0.5 m. Note that our model has no limitations to consider large-scale problems; however, to minimize computational time and to make the parametric study easier, small-scale problems are considered.

The simulations are performed on a computer with Intel i7-

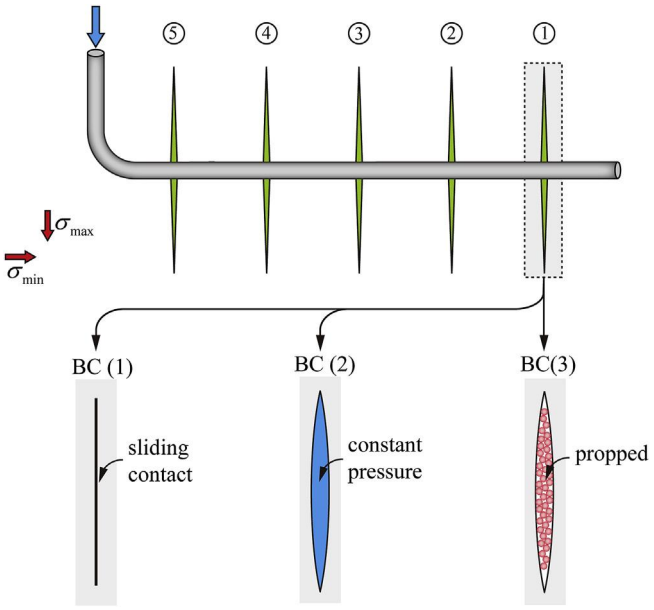

Fig. 11. Illustration of the sequential fracturing in a horizontal well (only two stages, i.e., Stage-1 and Stage-2 fractures, are simulated), as well as illustration of three boundary conditions applied on the Stage-1 fracture.

4790K 4.2 GHz processor and 8 GB DDR3 memory. It takes 11.9, 22.1 and 25.3 min for BC (1), BC (2) and BC (3), respectively. Fig. 12 shows the stress distributions in *x* direction after stage-1 fracture or stage-2 fracture reaches the target length of 20 m. In this paper, positive value of stress indicates compression. From Fig. 12(b1) we can notice that the shape of Stage-2 fracture is identical to Stage-1 fracture shown in Fig. 12(a) because, apparently, the Stage-1 fracture under BC (1) has no effect on its adjacent fracture. In Fig. 12(b2), the Stage-2 fracture is first attracted towards the tip of Stage-1 fracture, and then propagates towards the opposite side. In contrast to Fig. 12(b2), a quite distinct fracture path which totally curves away from Stage-1 fracture is shown in Fig. 12(b3).

In addition to the fracture propagation paths, the stress distributions under different boundary conditions are also quite distinct. Stage-1 fracture under BC (1) has no surrounding stress field, as clearly shown in Fig. 12(b1). The compressive stress near the center of Stage-1 fracture in Fig. 12(b3) is much stronger than that shown in Fig. 12(b2), and this difference is caused by the stress perturbation induced by the opening of a propped fracture. Besides, in Fig. 12(b2), the stress field is concentrated and strong around the opened tip of the stage-1 fracture whose surfaces are under the effect of uniform fluid pressure. As mentioned above, the stage-2 fracture is first attracted towards the tip of stage-1 fracture under the action of the near-tip stress filed, and then propagates away (leftwards) when exceeding the range of influence of the near-tip

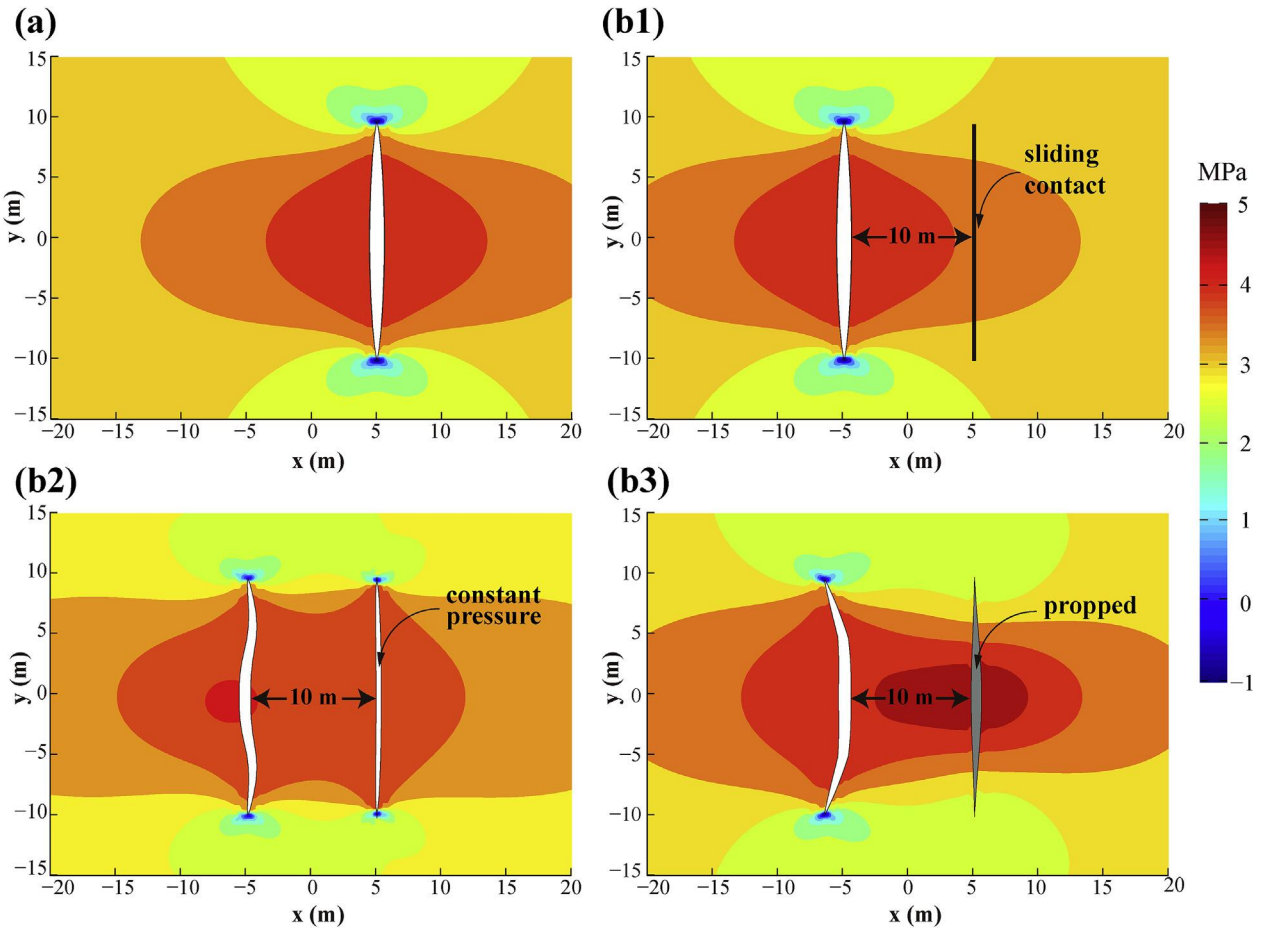

Fig. 12. (a) Stress distributions in *x*-direction after Stage-1 fracture reaches its target length. (b) Stress distributions in *x*-direction after Stage-2 fracture reaches its target length ((b1), (b2) and (b3) for boundary conditions (1), (2) and (3), respectively). Compressive stress is positive. Deformation is multiplied by a factor of 300 (similarly hereinafter).

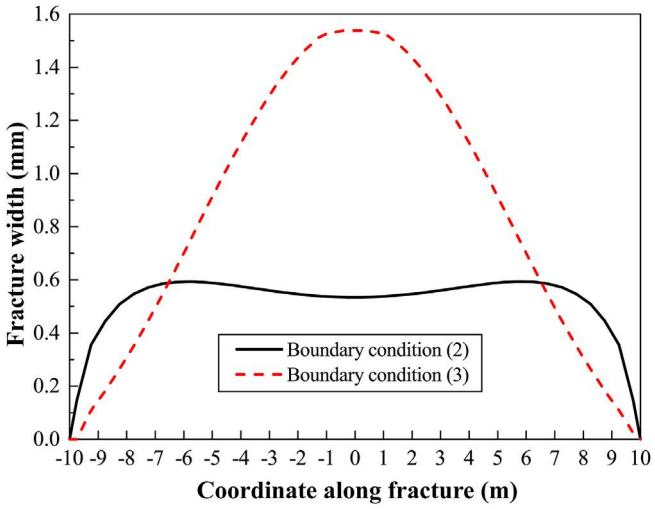

Fig. 13. Widths of Stage-1 fracture after the stage-2 fracture reaches its target length under boundary condition (2) and boundary condition (3).

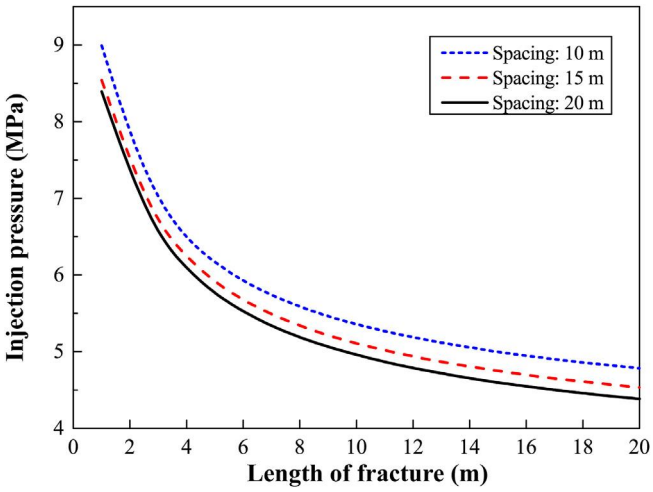

Fig. 15. Evolution of the injection pressures of Stage-2 fracture with different fracture spacings.

stress filed. In sharp contrast, for the situation in Fig. 12(b3), the proppant at a fairly low concentration near the fracture tip (see Fig. 10 for details) is not able to keep the fracture open and results in the closing of the fracture front, hence there is no singular stress field around the tip of Stage-1 fracture. As a consequence, the stage-2 fracture will not be attracted and the resulting propagation path is relatively simple compared with that in Fig. 12(b2).

The widths of Stage-1 fractures under BCs (2) and (3) are shown in Fig. 13, from which we can see that the fracture width under BC (3) is much wider than that under BC (2) (Stage-1 fracture under BC (1), which has zero width, is not shown here). Under the action of compressive stress caused by high fluid pressure inside the adjacent Stage-2 fracture, the width of Stage-1 fracture narrows down, especially near the central section, as the solid line shows. On the contrary, the existence of proppant keeps the Stage-1 fracture from closing, as the dashed line shows.

In fact, the comparison with other numerical simulation results (Kresse et al., 2013; Sesetty and Ghassemi, 2015) of sequential fracturing indicate that only the propagation path predicted by BC (3) is correct (Fig. 12(b3)). Therefore, we can see that the proper and accurate modeling of propped fractures is of great importance for simulators used to optimize the multistage fracturing design in the horizontal. Furthermore, it should be noted that when modeling the propped fracture using other numerical methods, additional elements such as joint elements should be added between the fracture surfaces (Sesetty and Ghassemi, 2015), which is not as convenient as the proposed method.

3.3. Sensitivity analysis

3.3.1. Effects of fracture spacing

In order to investigate the effects of fracture spacing on stress interference between fractures, hydraulic fracturing of two fractures with larger spacings of 15 m and 20 m under BC (3) are simulated. All the other parameters are kept the same as Section 3.2. From Fig. 14 (a), we can see that the stress shadow effect still has influence on the propagation of Stage-2 fracture when the spacing is 15 m. However, there is no deflection in the Stage-2 fracture path when the spacing equals 20 m, as shown in Fig. 14 (b), where the stress shadow effect is small at this distance.

The variation of injection pressures of Stage-2 fracture is shown in Fig. 15. As can be seen, the fluid pressure at the injection point increases as the spacing decreases, indicating that it is more difficult to create the closely spaced hydraulic fractures than the widely

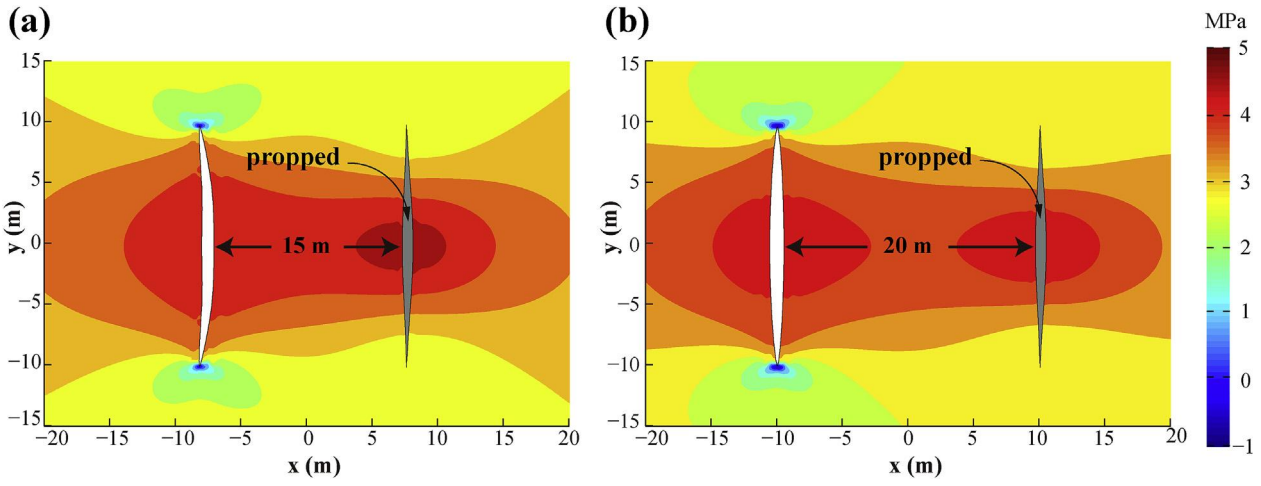

Fig. 14. Stress distributions in *x*-direction after Stage-2 fracture reaches its target length with spacings of 15 m (a) and 20 m (b).

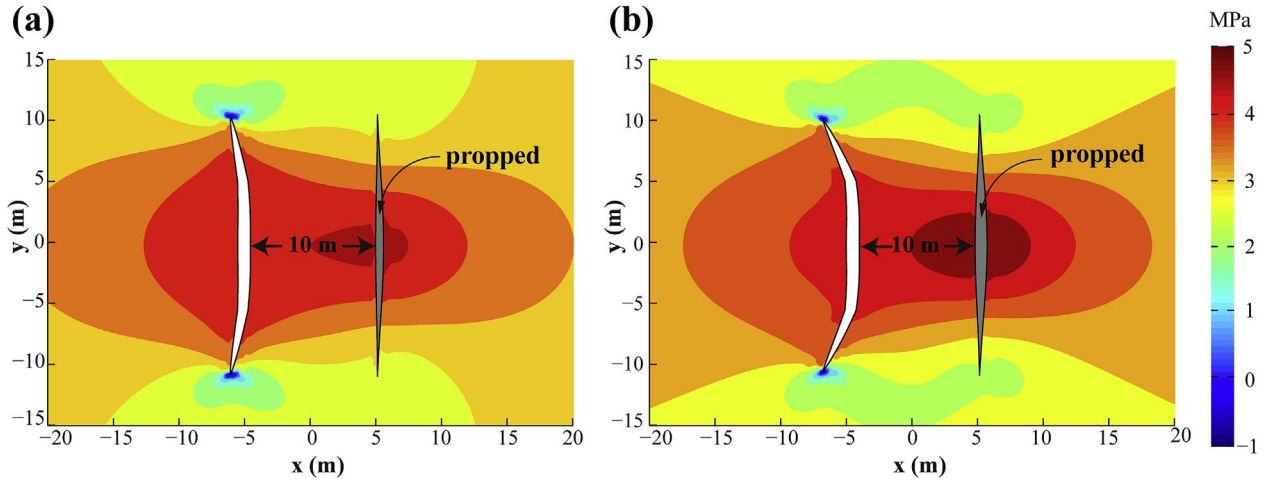

Fig. 16. Stress distributions in *x*-direction after Stage-2 fracture reaches its target length with $c_{max} = 0.3$ (a) and $c_{max} = 0.5$ (b).

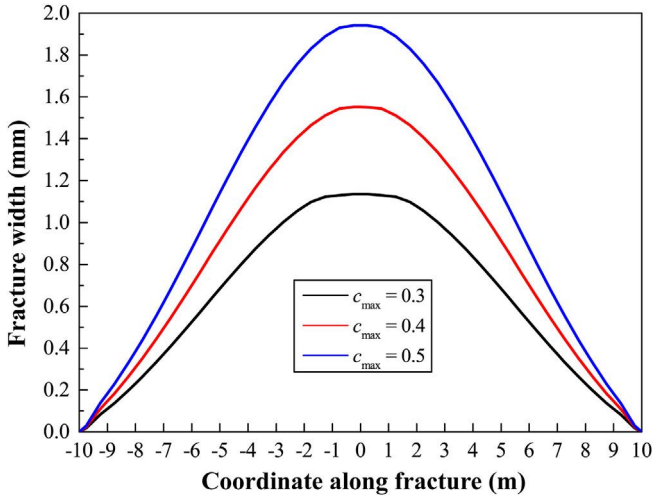

Fig. 17. Widths of the propped Stage-1 fracture after the stage-2 fracture reaches its target length with different c_{max}.

spaced ones.

3.3.2. Effects of proppant concentration of injected slurry

Hydraulic fracturing of two fractures with $c_{max} = 0.3$ and $c_{max} = 0.5$ under BC (3) are simulated to investigate the effects of proppant concentration of injected slurry. All the other parameters are kept the same as Section 3.2. From Fig. 16, we can see that c_{max} have obvious influence on propagation path of the stage-2 fracture. The extent of fracture path deviation increases as c_{max} increases, and this is caused by the fact that as c_{max} increases, the widths of the propped fracture increase, as shown in Fig. 17.

4. Conclusion

In this paper, we have presented an XFEM-based coupled numerical framework to model hydraulic fracturing problems in consideration of proppant. The proposed model was used to research the factors that influence the simulation results of sequential fracturing in a horizontal well. Based on the obtained simulation results, the following conclusions can be made:

(1) For the simulation of sequential fracturing, the fracture path of the subsequently created fracture is strongly affected by the boundary conditions applied on the previously created propped fracture. To obtain satisfactory simulation results, the widths of the propped fracture should be determined according to the distribution of proppant, and the propped fractures must be explicitly and properly modeled.
(2) Sensitivity analysis of fracture spacing shows that large injection pressure is needed when the fractures are spaced closely.
(3) Sensitivity analysis of proppant concentration of injected slurry shows that it influences both the fracture path and the stress distribution.

The advantages of XFEM make the proposed model an attractive tool for the design of multistage hydraulic fracturing in the horizontal well. Moreover, the proposed coupled approach can be applied to three-dimensional problems where the gravitational settling of proppant can be easily taken into consideration.

Acknowledgements

This work was jointly supported by National Natural Science Foundation of China (11472263, 11525211), Anhui Provincial Natural Science Foundation (1408085J08) and the Fundamental Research Funds for the Central Universities of China (WK2090050036).

Nomenclature

$\boldsymbol{a}$	Vector of enriched DOF associated with Heaviside function
$\boldsymbol{b}$	Vector of enriched DOF associated with tip enrichment function
$\boldsymbol{B}$	Matrix of shape function derivatives
c	Proppant volumetric concentration
c_{inj}	Proppant volumetric concentration at the injection point
c_{last}	Proppant volumetric concentration of the last time step
c_{max}	Maximum proppant volumetric concentration of the injected slurry
$\hat{c}$	Saturation volumetric concentration
C_L	Carter's leak-off coefficient
$\boldsymbol{D}$	Elastic tensor
E	Elastic modulus

f_s, f_p	Non-dimensional functions
F_l	Tip enrichment functions
$\boldsymbol{F}$	Force vector
g_L	Leak-off rate of fluid into the rock formation
$\boldsymbol{G}$	Leak-off term in the coupled equations
H	Heaviside function
$\boldsymbol{H}$	Global flux stiffness of fluid elements
$\boldsymbol{J}$	Jacobian matrix of NR iteration
k	Permeability of fracture
$\boldsymbol{K}$	Global stiffness matrix
m	Exponent for the calculation of dynamic viscosity
N	Standard finite element shape functions
N^p	Shape functions of fluid element
$\boldsymbol{N}^p,\boldsymbol{N}^u,\boldsymbol{N}^w$	Matrices of shape functions
p	Fluid pressure
$\boldsymbol{p}$	Fluid pressure vector
q_p	Proppant flux
q_s	Slurry flux
$\boldsymbol{Q}$	Matrix transferring fluid pressure into equivalent nodal forces
$\boldsymbol{R}$	Residual vector of NR iteration
s	Coordinate system along hydraulic fracture
s_{tip}	Location of fracture tip
S_{frac}	Set of nodes whose support domains are fully cut by fracture
S_{tip}	Set of nodes whose support domains are partially cut by fracture
$\boldsymbol{S}$	Source term in coupled equations
t	Time
Δt	Time increment
Q	Injection rate of slurry
K_I, K_{II}	Mode-I and Mode-II stress intensity factors
K_e	Equivalent stress intensity factor
K_{IC}	Fracture toughness
K_m	Dimensionless fracture toughness
$\boldsymbol{u}$	Displacement vector
$\boldsymbol{u}^+$	Displacement vector of nodes on the positive fracture face
$\boldsymbol{u}^-$	Displacement vector of nodes on the negative fracture face
$\boldsymbol{U}$	Global nodal displacement
w	Fracture width
w_o	Fracture width before fracture starts to close
w_p	Width of propped fracture
$\boldsymbol{w}$	Fracture width vector
$\boldsymbol{W}$	A vector formed by widths of nodes on fracture surface
$\beta_0, \beta_1, \beta_2$	Variables in multipoint constraint condition (Eq. (24))
$\boldsymbol{\sigma}$	Stress tensor
$\boldsymbol{\varepsilon}$	Strain tensor
ε_{tol}^w	Convergence tolerance
η	Packing density of proppant pack
ν	Poisson's ratio
μ	Fluid viscosity
χ	A variable in Eq. (26)
θ	Fracture propagation angle in the local fracture tip coordinate system
γ	Inclination of fracture

Appendix A. Weak form and discretization of governing equations

After introducing the trial function $\boldsymbol{u}$ and test functions $\delta\boldsymbol{u}$ for the displacement field, the weak form of equilibrium equation (Eq. (1)) can be expressed as

$$\int_{\Omega} \delta\boldsymbol{\varepsilon} : \boldsymbol{\sigma} \mathrm{d}\Omega - \int_{\Gamma_t} \delta\boldsymbol{u}\cdot\boldsymbol{t}\mathrm{d}\Gamma + \int_{\Gamma_{frac}^+} \delta\boldsymbol{u}^+\cdot p\boldsymbol{n}_{\Gamma_{frac}}\mathrm{d}\Gamma - \int_{\Gamma_{frac}^-} \delta\boldsymbol{u}^-\cdot p\boldsymbol{n}_{\Gamma_{frac}}\mathrm{d}\Gamma = 0 \tag{A.1}$$

Because $\boldsymbol{p} = p\boldsymbol{n}_{\Gamma_{frac}}$ and $\boldsymbol{w} = \boldsymbol{n}_{\Gamma_{frac}}\cdot(\boldsymbol{u}^+ - \boldsymbol{u}^-)\cdot\boldsymbol{n}_{\Gamma_{frac}}$, Eq. (A.1) can be further written as

$$\int_{\Omega} \delta\boldsymbol{\varepsilon} : \boldsymbol{\sigma} \mathrm{d}\Omega - \int_{\Gamma_t} \delta\boldsymbol{u}\cdot\boldsymbol{t}\mathrm{d}\Gamma + \int_{\Gamma_{frac}} \delta\boldsymbol{w}\cdot\boldsymbol{p}\mathrm{d}\Gamma = 0 \tag{A.2}$$

By introducing any allowable test function δp, the weak form of the Reynolds equation (Eq. (14)) can be expressed as

$$\int_{\Gamma_{frac}} \left(\delta p\frac{\partial w}{\partial t} + \frac{\partial(\delta p)}{\partial s}k\frac{\partial p}{\partial s} + \delta p g_L\right)\mathrm{d}\Gamma + \delta pQ|_{Bu} = 0 \tag{A.3}$$

where Bu represents the boundary conditions of flow, as given in Eq. (16).

The finite element approximation of pressure field inside the fracture can be expressed as

$$p(s) = \sum_{i\in S_{hf}} N_i^p(s)p_i \equiv \boldsymbol{N}^p(s)\boldsymbol{p} \tag{A.4}$$

where S_{hf} is the nodes set of the fluid elements defined along the hydraulic fracture. $N_i^p(s)$ represents the shape function of pressure p_i for node i. $\boldsymbol{p}$ is the nodal pressure vector and $\boldsymbol{N}^p(s)$ is the matrix of shape functions defined in the natural local coordinate system ξ, that is

$$\begin{cases} N_1^p(\xi) = (\xi-1)/2 \\ N_2^p(\xi) = (\xi+1)/2 \end{cases} \tag{A.5}$$

The fracture opening displacement vector $\boldsymbol{w}$ can be approximated by

$$\boldsymbol{w}(s) = \sum_{i\in S_w} N_i^w(s)\boldsymbol{u}_i \equiv \boldsymbol{N}^w(s)\boldsymbol{U} \tag{A.6}$$

where S_w is the nodes set of element that contains point s, $\boldsymbol{N}_i^w(s)$ is the shape function matrix of the fracture opening displacement and $\boldsymbol{U}$ is the global nodal displacement vector.

By substituting the displacement and pressure approximations (Eqs. (18), (A.4) and (A.6)) and the linear elastic constitutive equation (Eq. (3)) into the weak form of the equilibrium equation (Eq. (A.2)) and the Reynolds equation (Eq. (A.3)), the discretized equilibrium and flow continuity equations can be written as

$$\boldsymbol{K}\boldsymbol{U} - \boldsymbol{Q}\boldsymbol{P} - \boldsymbol{F} = \boldsymbol{0} \tag{A.7}$$

$$\boldsymbol{Q}^T\Delta\boldsymbol{U} + \Delta t\boldsymbol{H}\boldsymbol{P} + \Delta t\boldsymbol{S} - \Delta t\boldsymbol{G} = \boldsymbol{0} \tag{A.8}$$

In Eq. (A.7), the global stiffness matrix $\boldsymbol{K}$, the matrix $\boldsymbol{Q}$ that transfers fluid pressure $\boldsymbol{P}$ into equivalent nodal forces and the load vector $\boldsymbol{F}$ are defined as

$$\boldsymbol{K} = \int_{\Omega} \boldsymbol{B}^T\boldsymbol{D}\boldsymbol{B}\mathrm{d}\Omega \tag{A.9}$$

$$\boldsymbol{Q} = \int_{\Omega} (\boldsymbol{N}^{w})^{T} \boldsymbol{D} \boldsymbol{N}^{p} \mathrm{d}\Omega \tag{A.10}$$

$$\boldsymbol{F} = \int_{\Gamma_t} (\boldsymbol{N}^{u})^{T} \boldsymbol{t} \mathrm{d}\Gamma \tag{A.11}$$

where $\boldsymbol{B}$ is the matrix of shape function derivatives. In Eq. (A.8), Δt is the time increment between two adjacent time steps, the matrix $\boldsymbol{H}$, the source term $\boldsymbol{S}$ and the leak-off term $\boldsymbol{G}$ are defined as

$$\boldsymbol{H} = \int_{\Gamma_{frac}} \left(\frac{\partial \boldsymbol{N}^{p}}{\partial s}\right)^{T} k \frac{\partial \boldsymbol{N}^{p}}{\partial s} \mathrm{d}s \tag{A.12}$$

$$\boldsymbol{S} = \boldsymbol{N}^{p}(s)^{T}|_{s=0} Q(t) \tag{A.13}$$

$$\boldsymbol{G} = \int_{\Gamma_{frac}} (\boldsymbol{N}^{p})^{T} g_{L}(s) \mathrm{d}s \tag{A.14}$$

Appendix B. Newton-Raphson iteration

The Newton-Raphson method is adopted to solve the coupled equations (Eq. (25)) at each time step. For this purpose, the residual vector $\boldsymbol{R}^{\tilde{i}}$ at iteration step $\tilde{i}$ can be defined as

$$\boldsymbol{R}^{\tilde{i}} = \begin{bmatrix} \boldsymbol{0} & \boldsymbol{0} \\ -\boldsymbol{Q}^{T} & \boldsymbol{0} \end{bmatrix} \begin{pmatrix} \Delta \boldsymbol{U} \\ \Delta \boldsymbol{P} \end{pmatrix}^{\tilde{i}} + \begin{bmatrix} \boldsymbol{K} & -\boldsymbol{Q} \\ \boldsymbol{0} & -\Delta t \boldsymbol{H}^{\tilde{i}} \end{bmatrix} \begin{pmatrix} \boldsymbol{U} \\ \boldsymbol{P} \end{pmatrix}^{\tilde{i}} - \begin{pmatrix} \boldsymbol{F} \\ \Delta t \boldsymbol{S}^{\tilde{i}} - \Delta t \boldsymbol{G}^{\tilde{i}} \end{pmatrix}^{\tilde{i}} \tag{B.1}$$

and the Jacobian matrix of residual $\boldsymbol{R}^{\tilde{i}}$ can be obtained by

$$\boldsymbol{J}^{\tilde{i}} = \begin{bmatrix} \boldsymbol{K} & -\boldsymbol{Q} \\ -\boldsymbol{Q}^{T} & -\Delta t \boldsymbol{H}^{\tilde{i}} \end{bmatrix} \tag{B.2}$$

then the displacement $\boldsymbol{U}$ and the fluid pressure $\boldsymbol{P}$ can be updated according to

$$\begin{pmatrix} \boldsymbol{U} \\ \boldsymbol{P} \end{pmatrix}^{\tilde{i}+1} = \begin{pmatrix} \boldsymbol{U} \\ \boldsymbol{P} \end{pmatrix}^{\tilde{i}} - \frac{\boldsymbol{R}^{\tilde{i}}}{\boldsymbol{J}^{\tilde{i}}} \tag{B.3}$$

The convergence criterion for the Newton-Raphson iteration can be written as

$$\frac{\left\| \boldsymbol{w}^{\tilde{i}} - \boldsymbol{w}^{\tilde{i}-1} \right\|}{\left\| \boldsymbol{w}^{\tilde{i}-1} \right\|} \leq \varepsilon_{tol}^{w} \tag{B.4}$$

where "$\|\|$" is the 2-norm operator, ε_{tol}^{w} is the convergence tolerance and is taken as 1×10^{-3} in this paper, and $\boldsymbol{w}^{\tilde{i}}$ is the fracture width at the $\tilde{i}\_th$ iteration step.

References

Adachi, J., Siebrits, E., Peirce, A., Desroches, J., 2007. Computer simulation of hydraulic fractures. Int. J. Rock Mech. Min. Sci. 44 (5), 739–757.

Batchelor, G.K., 1967. An Introduction to Fluid Dynamics. Cambridge University Press, Cambridge.

Bose, C.C., Fairchild, B., Jones, T., Gul, A., Ghahfarokhi, R.B., 2015. Application of nanoproppants for fracture conductivity improvement by reducing fluid loss and packing of micro-fractures. J. Nat. Gas Sci. Eng. 27, 424–431.

Britt, L., 2012. Fracture stimulation fundamentals. J. Nat. Gas Sci. Eng. 8, 34–51.

Carrier, B., Granet, S., 2012. Numerical modeling of hydraulic fracture problem in permeable medium using cohesive zone model. Eng. Fract. Mech. 79, 312–328.

Carter, R.D., 1957. Derivation of the General Equation for Estimating the Extent of the Fractured Area, Drilhng and Production Practices. American Petroleum Institute, Dallas, pp. 261–270.

Chandrupatla, T.R., Belegundu, A.D., Ramesh, T., Ray, C., 2012. Introduction to Finite Elements in Engineering. Prentice Hall, New Jersey.

Chen, Z., 2012. Finite element modelling of viscosity-dominated hydraulic fractures. J. Petrol. Sci. Eng. 88–89, 136–144.

Chen, Z., Dongarra, J., Luszczek, P., Roche, K., 2003. Self-adapting software for numerical linear algebra and LAPACK for clusters. Parallel Comput. 29 (11–12), 1723–1743.

Dahi-Taleghani, A., Olson, J.E., 2011. Numerical modeling of multistranded-hydraulic-fracture propagation: accounting for the interaction between induced and natural fractures. SPE J. 16 (3), 575–581.

Daneshy, A.A., 1978. Numerical solution of sand transport in hydraulic fracturing. J. Petrol. Technol. 30, 132–140.

Daux, C., Moës, N., Dolbow, J., Sukumar, N., Belytschko, T., 2000. Arbitrary branched and intersecting cracks with the extended finite element method. Int. J. Numer. Methods Eng. 48 (12), 1741–1760.

Detournay, E., 2004. Propagation regimes of fluid-driven fractures in impermeable rocks. Int. J. Geomech. 4 (1), 35–45.

Dontsov, E.V., Peirce, A.P., 2015. Proppant transport in hydraulic fracturing: crack tip screen-out in KGD and P3D models. Int. J. Solids Struct. 63, 206–218.

Erdogan, F., Sih, G.C., 1963. On the crack extension in plates under plane loading and transverse shear. J. Basic Eng. 85 (4), 519–525.

Gordeliy, E., Peirce, A., 2013. Coupling schemes for modeling hydraulic fracture propagation using the XFEM. Comput. Methods Appl. Mech. Eng. 253, 305–322.

Guo, J., Zhao, X., Zhu, H., Zhang, X., Pan, R., 2015a. Numerical simulation of interaction of hydraulic fracture and natural fracture based on the cohesive zone finite element method. J. Nat. Gas Sci. Eng. 25, 180–188.

Guo, T., Zhang, S., Zou, Y., Xiao, B., 2015b. Numerical simulation of hydraulic fracture propagation in shale gas reservoir. J. Nat. Gas Sci. Eng. 26, 847–856.

Hammond, P.S., 1995. Settling and slumping in a Newtonian slurry, and implications for proppant placement during hydraulic fracturing of gas wells. Chem. Eng. Sci. 50 (20), 3247–3260.

Hirsch, C., 1990. Numerical Computation of Internal and External Flows. In: Computational Methods for Inviscid and Viscous Flows, vol. 2. John Wiley & Sons, New York.

Hu, J., Garagash, D.I., 2010. Plane-strain propagation of a fluid-driven crack in a permeable rock with fracture toughness. J. Eng. Mech. 136 (9), 1152–1166.

Kresse, O., Weng, X., Gu, H., Ruiting, W., 2013. Numerical modeling of hydraulic fractures interaction in complex naturally fractured formations. Rock Mech. Rock Eng. 46 (3), 555–568.

Lecampion, B., 2009. An extended finite element method for hydraulic fracture problems. Commun. Numer. Methods Eng. 25 (2), 121–133.

Liu, C., Liu, H., Zhang, Y., Deng, D., Wu, H., 2015. Optimal spacing of staged fracturing in horizontal shale-gas well. J. Petrol. Sci. Eng. 132, 86–93.

Mansoor, Z., 2015. Application of polymers for coating of proppant in hydraulic fracturing of subterraneous formations: a comprehensive review. J. Nat. Gas Sci. Eng. 24, 197–209.

McClure, M.W., Horne, R.H., 2013. Discrete Fracture Network Modeling of Hydraulic Stimulation: Coupling Flow and Geomechanics. Springer, Berlin.

Moës, N., Dolbow, J., Belytschko, T., 1999. A finite element method for crack growth without remeshing. Int. J. Numer. Methods Eng. 46 (1), 131–150.

Mohammadnejad, T., Khoei, A.R., 2013. An extended finite element method for hydraulic fracture propagation in deformable porous media with the cohesive crack model. Finite Elem. Anal. Des. 73, 77–95.

Moran, B., Shih, C.F., 1987. Crack tip and associated domain integrals from momentum and energy balance. Eng. Fract. Mech. 27 (6), 615–642.

Ouyang, S., Carey, C.F., Yew, C.H., 1997. An adaptive finite element scheme for hydraulic fracturing with proppant transport. Int. J. Numer. Methods Fluids 24 (7), 645–670.

Papanastasiou, P., 1999. An efficient algorithm for propagating fluid-driven fractures. Comput. Mech. 24 (4), 258–267.

Queipo, N.V., Verde, A.J., Canelon, J., Pintos, S., 2002. Efficient global optimization for hydraulic fracturing treatment design. J. Petrol. Sci. Eng. 35 (3–4), 151–166.

Rivers, M., Zhu, D., Hill, A.D., 2012. Proppant fracture conductivity with high proppant loading and high closure stress. In: SPE Hydraulic Fracturing Technology Conference. Society of Petroleum Engineers, The Woodlands, Texas, United states, pp. 196–205.

Sesetty, V., Ghassemi, A., 2015. A numerical study of sequential and simultaneous hydraulic fracturing in single and multi-lateral horizontal wells. J. Petrol. Sci. Eng. 132, 65–76.

Steinhaus, H., 1999. Mathematical Snapshots. Dover Publications, New York.

Stolarska, M., Chopp, D.L., Moës, N., Belytschko, T., 2001. Modelling crack growth by level sets in the extended finite element method. Int. J. Numer. Methods Eng. 51 (8), 943–960.

Sukumar, N., Prevost, J.H., 2003. Modeling quasi-static crack growth with the extended finite element method Part I: computer implementation. Int. J. Solids Struct. 40 (26), 7513–7537.

Sun, J., Schechter, D.S., 2015. Optimization-based unstructured meshing algorithms for simulation of hydraulically and naturally fractured reservoirs with variable

distribution of fracture aperture, spacing, length and strike. SPE Reserv. Eval. Eng. 18 (04), 463–480.
Tomac, I., Gutierrez, M., 2013. Numerical study of horizontal proppant flow and transport in a narrow hydraulic fracture. In: 47th U.S. Rock Mechanics/Geomechanics Symposium. American Rock Mechanics Association, San Francisco, California.
Wangen, M., 2011. Finite element modeling of hydraulic fracturing on a reservoir scale in 2D. J. Petrol. Sci. Eng. 77 (3–4), 274–285.
Weng, X., Kresse, O., Chuprakov, D., Cohen, C.-E., 2014. Applying complex fracture model and integrated workflow in unconventional reservoirs. J. Petrol. Sci. Eng. 124, 468–483.
Wrobel, L.C., Aliabadi, M.H., 2002. The Boundary Element Method. John Wiley & Sons, New York.
Zhang, X., Jeffrey, R.G., 2006. The role of friction and secondary flaws on deflection and re-initiation of hydraulic fractures at orthogonal pre-existing fractures. Geophys. J. Int. 166 (3), 1454–1465.
Zhou, L., Hou, M.Z., Gou, Y., Li, M., 2014. Numerical investigation of a low-efficient hydraulic fracturing operation in a tight gas reservoir in the North German Basin. J. Petrol. Sci. Eng. 120, 119–129.